Available online at www.sciencedirect.com
ScienceDirect
Journal of Catalysis 254 (2008) 144–155
JOURNAL OF CATALYSIS
www.elsevier.com/locate/jcat

Topotactic synthesis of mesoporous ZnS and ZnO nanoplates and their photocatalytic activity

Jum Suk Jang [a], Chung-Jong Yu [b], Sun Hee Choi [b], Sang Min Ji [a], Eun Sun Kim [a], Jae Sung Lee [a,*]

[a] *Eco-friendly Catalysis and Energy Laboratory (NRL), Department of Chemical Engineering and School of Environmental Science and Engineering, Pohang University of Science and Technology (POSTECH), San 31, Hyojadong, Namgu, Pohang 790-784, Republic of Korea*
[b] *Beamline Research Division, Pohang Accelerator Laboratory, POSTECH, San 31, Hyojadong, Namgu, Pohang 790-784, Republic of Korea*

Received 10 August 2007; revised 9 November 2007; accepted 16 December 2007

Available online 8 January 2008

Abstract

Mesoporous ZnS and ZnO nanoplates were fabricated by calcination of a $ZnS(en)_{0.5}$ complex (en = ethylenediamine), which was solvothermally synthesized using ethylenediamine as a single solvent. When the synthesized $ZnS(en)_{0.5}$ complex was heated, mesoporous nanoplates of wurtzite ZnS were formed, which then transformed to ZnO platelets upon further oxidation. The $ZnS(en)_{0.5} \rightarrow ZnS \rightarrow ZnO$ transformation process appeared to be topotatic because of the crystallographic relation of the structures and pseudomorphism among the three solids. Photocatalytic performance of the materials was investigated for hydrogen production from aqueous Na_2S/Na_2SO_3 solution and decomposition of the azo dye, acid red 14. The ZnS calcined at 500 °C exhibited the highest hydrogen production rate through water splitting under visible light irradiation, and ZnO calcined at 550–600 °C photocatalytically degraded the dye upon UV-irradiation.

Keywords: Solvothermal synthesis; Mesoporous ZnS and ZnO nanoplates; Topotactic transformation; Photocatalysts

1. Introduction

Zinc sulfide (ZnS) is a wide-band gap semiconductor with a band gap energy of 3.80 eV for the hexagonal wurtzite phase and of 3.66 eV for the cubic zinc-blende phase. It has a wide range of optical properties with various dopants such as Tb and Eu [1]. ZnS nanocrystals also show activity for the photocatalytic decomposition of organic materials due to trapped holes arising from surface defects on the sulfide [2,3]. Similarly, ZnO is one of the most important functional oxides for optoelectronics and photocatalysis, with a band gap energy of 3.20 eV. It has been demonstrated to have potential applications as nanosized sensors and field-effect transistors [4,5], and as a photocatalyst for the degradation of organic dyes [6–9].

The applications of nanostructured ZnS and ZnO are dictated by their morphology and textural properties such as surface area and porosity. While one-dimensional nanowires and nanorods have been extensively studied, two-dimensional (2D) nanostructured materials have attracted much less attention until recently. However, 2D nanomaterials show strong potential as chemical and biological sensors, nanoelectronic devices, and catalysts with their high surface areas and large pore volumes. Thus, ZnS nanosheets have been successfully prepared through a solvothermal route [10–15]. Ethylenediamine was used as a liquid medium and a structure-directing, coordinating molecular template that led to a particular morphology of product.

Mesoporous materials with high surface areas have also been widely used in photocatalysis for the purpose of eliminating environmental hazards [16–20]. Nevertheless, the high preparation cost of such mesoporous materials has been considered an obstacle to overcome. Hue et al. recently reported that a precursor thermolysis provided a low-cost self-assembly route to mesoporous ZnS nanoparticles with a high ratio of surface to volume and that aggregation of nanoparticles was avoided during the photocatalytic reaction of dyes [21]. However, no study has been reported yet for porous ZnS and ZnO with other morphologies.

* Corresponding author. Fax: +82 562 279 5799.
E-mail address: jlee@postech.ac.kr (J.S. Lee).

0021-9517/$ – see front matter
doi:10.1016/j.jcat.2007.12.010

In this contribution, we prepared the $ZnS(en)_{0.5}$ complex precursor by a solvothermal route using ethylenediamine (en) as a single solvent and obtained porous ZnS and ZnO nanoplates through thermal treatment of the complex. We investigated the chemical changes accompanying the transformation of the materials using diverse spectroscopic tools. In particular, the local structures in the platelets were elucidated with the synchrotron radiation techniques of powder X-ray diffraction (XRD) and X-ray absorption fine structure (XAFS). Photocatalytic water splitting and photocatalytic degradation of an organic dye were performed in order to measure the catalytic performance of the synthesized $ZnS(en)_{0.5}$ complex and its derivatives.

2. Experimental

2.1. Preparation of host materials

For solvothermal synthesis, 16.2 mmol $Zn(NO_3)_2 \cdot 6H_2O$ and 48.6 mmol thiourea NH_2CSNH_2 were added to a Teflon-lined stainless steel autoclave which had been filled with ethylenediamine $NH_2(CH_2)_2NH_2$ to 70% of its volume. The autoclave reactor was maintained at 160 °C for 12 h and then allowed to cool to room temperature. The colored precipitate was filtered and washed with absolute ethanol and deionized water to remove the residual impurities such as organic solvent; then it was dried in an oven at 80 °C for 12 h. Samples of the obtained $ZnS(en)_{0.5}$ complex precursor were calcined at 400, 500, 550, and 600 °C for 2 h in an electrical furnace under ambient air; these samples are denoted Zn400, Zn500, Zn550, and Zn600, respectively. Commercial ZnS (Aldrich, 99.99%) and ZnO (Junsei, 99%) were also employed for comparison.

2.2. Characterization with synchrotron radiation techniques

The crystalline phases of the materials were determined by synchrotron radiation powder X-ray diffraction (SR-XRD). The SR-XRD patterns were taken at the 8C2 high resolution powder diffraction beamline of Pohang Accelerator Laboratory (PAL) in Pohang, Korea. Scintillation detectors were rotated at a step of 0.01° around a flat sample stage, which was spinning to realize randomness of planes in materials during X-ray measurements.

The electronic and local geometric structures around Zn in the materials were characterized with XAFS. X-ray absorption measurements were conducted at the 7C1 beamline of PAL (2.5 GeV; stored current of 130–180 mA). After calcination at the desired temperatures, the materials were cooled to room temperature, and their spectra taken in transmission mode. The radiation was monochromatized using a Si(111) double crystal monochromator, with the incident beam detuned by 15% to minimize contamination from higher harmonics.

The data obtained were analyzed using the IFEFFIT suite of software programs [22] and the FEFF 8.2 code [23]. The detailed procedure for data analysis is described elsewhere [24–26]. The pre-edge background was removed using a simple linear fit. The post-edge background function was approximated with a piecewise spline that could be adjusted so that the low-R components of pre-Fourier transformed data would be minimized. After calculation of the extended X-ray absorption fine structure (EXAFS) function, k^3-weighted $\chi(k)$ in momentum (k) space was Fourier transformed to obtain the radial structural function (RSF) in R space. A shell of interest in the RSF was back-transformed into the momentum space. The FEFF code was used to generate theoretical data for a given structure so that the individual contribution of a specific absorber-backscatterer could be distinguished.

2.3. Other characterizations

The morphologies of the as-synthesized and calcined materials were investigated by SEM (Hitachi, S-4200) and TEM (JEOL JEM 2010F) operated at 200 kV. A differential scanning calorimeter (DSC) (Shimadzu, DTA-50) was used to monitor changes during the thermal treatment of the $ZnS(en)_{0.5}$ complex. The DSC curves were recorded in the temperature range of 50–800 °C at a heating rate of 10 °C/min under a 45 mL/min air flow. A Jasco Valor-III spectrometer was used to take FT-IR spectra of disk-type samples prepared by mixing with KBr. The C, N, and H contents of each sample were analyzed by an elemental analyzer (Analysensysteme GmbH, Valio EL).

To investigate the physical texture of the calcined materials, measurements of N_2 adsorption–desorption isotherms at 77 K were performed in a constant-volume adsorption apparatus (Micrometrics ASAP 2010) at relative pressures (P/P_0) ranging from 10^{-4} to 0.995. Before the measurement of N_2 adsorption–desorption isotherms, the samples were degassed for 4 h at 393 K under 10^{-4} Torr. The specific surface area was calculated using the Brunauer–Emmett–Teller (BET) method [27] and the pore size distribution (PSD) was calculated from nitrogen desorption data using the Barrett–Joyner–Halenda (BJH) method with the modified Kelvin equation [28]. The pore volume was assessed on the basis of the adsorbed amount at a relative pressure (P/P_0) of 0.99.

2.4. Photocatalytic reaction procedures

Photocatalytic hydrogen production was performed at room temperature under atmospheric pressure in a closed circulation system using an Hg-arc lamp (500 W) equipped with a UV cut-off filter ($\lambda \geqslant 420$ nm). The rate of H_2 evolution was determined for an aqueous 0.1 M Na_2S + 0.02 M Na_2SO_3 solution (100 ml) containing 0.1 g catalyst. Platinum was loaded (1 wt% Pt) on the samples by an impregnation method. To investigate the rate of hydrogen evolution vs. the wavelengths we used different cutoff filters (with the wavelength tolerance of ±10 nm) of 350, 385, 400, 420, 455, 475, 495, 515, and 550 nm wavelengths. The concentration of H_2 was analyzed by gas chromatography equipped with a thermal conductivity detector (molecular sieve 5-Å column and Ar carrier).

For decomposition of an azo dye, acid red 14 (AR14), 100 mL of 50 μM AR14 and 50 mg of photocatalysts were stirred for 30 min in a glass reactor prior to illumination. A 450-W Hg arc lamp (Oriel) was used as a light source. Light

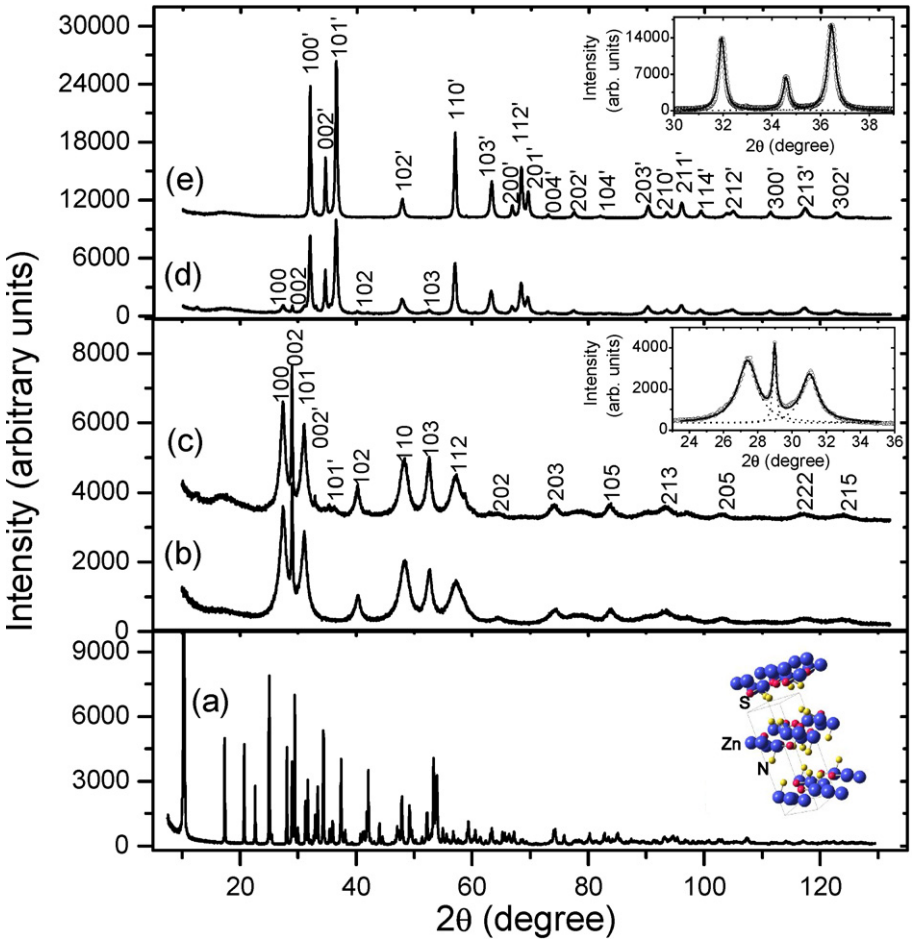

Fig. 1. SR-XRD patterns of (a) the $ZnS(en)_{0.5}$ complex and (b) Zn400, (c) Zn500, (d) Zn550, and (e) Zn600; its derivatives calcined at the indicated temperatures (°C). The insets show three strong peaks from Zn400 and Zn600 with fitting (—) to three Lorentzian curves (···).

passed through an IR water filter and a cutoff filter ($\lambda > 324$, 385, 420 nm), and then the filtered light was focused onto the reactor. Sample aliquots were withdrawn with a 1-mL syringe intermittently during the illumination, and then filtered through a 0.45-μm PTFE filter (Milipore). The degradation of AR 14 was monitored by measuring the maximum absorbance around a wavelength of 515 nm as a function of irradiation time with a UV–vis spectrophotometer.

3. Results and discussion

3.1. Topotatic transformation of the $ZnS(en)_{0.5}$ complex to ZnS and ZnO

The solvothermal reaction of the zinc precursor with thiourea in ethylenediamine (en) solvent yielded the $ZnS(en)_{0.5}$ complex having orthorhombic structure shown in Fig. 1a. The SR-XRD pattern of the complex agreed well with the known structure, in which ZnS layers are connected to each other through the bonding of the nitrogen atoms in ethylenediamine along the a-axis as shown in the inset of Fig. 1a [29].

When the $ZnS(en)_{0.5}$ complex was thermally treated, its crystal structure changed completely. Fig. 1b–d displays SR-XRD patterns of the $ZnS(en)_{0.5}$ derivatives: (b) Zn400, (c) Zn500, (d) Zn550 and (e) Zn600. The number in the notation denotes the calcination temperature in Celsius. The Zn400 was identified as hexagonal wurtzite ZnS, as shown in Fig. 1b, and the peak indices are the same as the unprimed indices in Fig. 1c. The three strong peaks in the low angle region were fitted to three Lorentzian curves as shown in the inset of the middle plane in Fig. 1. The particle or domain size of wurtzite ZnS (JCPDS card no. 36-1450) could be estimated as ca. 7 nm in the (100) direction and ca. 39 nm in the (001) direction using Scherrer's formula, $L \sim \lambda/\Delta(2\theta)\cos\theta$, where $\Delta(2\theta)$ is the full width at half maximum of the peak of the Lorentzian fit [30,31]. Preferential growth in the c-direction was noted.

Calcination at 500 °C for 2 h made the wurtzite ZnS peaks slightly sharper, as shown in Fig. 1c with an indication of two zincite ZnO peaks denoted with primed indices in the range of 30–40° in 2θ. Fig. 1d shows an XRD pattern of Zn550 with peak indices corresponding to those of hexagonal ZnO (JCPDS card no. 36-1451); the indices are the same as the primed ones shown in Fig. 1e for Zn600 although there are some wurtzite ZnS peaks left with unprimed peak indices. No significant preferential growth was found in Zn550 from the analysis of the particle size, which was ca. 22 nm in the (100) direction and ca. 28 nm in the (001) direction. Fig. 1e for Zn600 does not show wurtzite ZnS peaks at all, and the particle size has in-

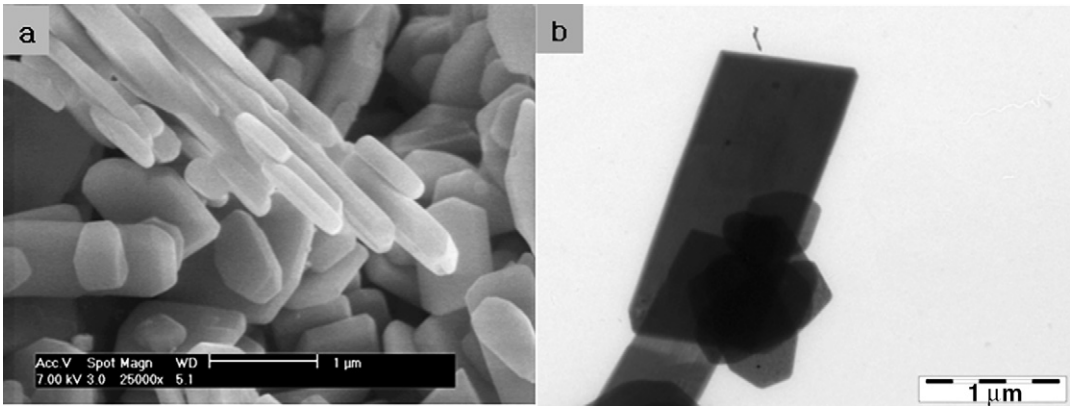

Fig. 2. (a) SEM and (b) TEM images of the $ZnS(en)_{0.5}$ complex.

Table 1
The C, N, and H contents of samples determined from elemental analysis

Samples	Elements			Total content (%)
	N	C	H	
$ZnS(en)_{0.5}$	11.0	10.2	3.4	24.6
Zn400	1.1	2.1	1.2	4.4
Zn500	0.37	0.57	0.66	1.60
Zn600	0.08	0.03	0.33	0.44

creased to ca. 35 nm in the (100) direction and ca. 39 nm in the (001) direction.

Fig. 2 shows SEM and TEM images of the $ZnS(en)_{0.5}$ complex. The precursor has a plate-like morphology with a lateral dimension in the range of $1 \sim 2$ μm. Elemental analysis was also employed to determine the C, N, and H contents of each sample. Table 1 shows that the composition of the precursor can be expressed by the formula $ZnS(NH_2CH_2CH_2NH_2)_{0.5}$ and that the calcined samples contain some residual organic matter. The percentages of C, H and N elements were C (10.15 wt%), H (3.38 wt%), and N (11.04 wt%) for $ZnS(en)_{0.5}$ precursors; their sum (24.57 wt%) is also consistent with the theoretical content (23.62 wt%) of ethylenediamine in the complex [11]. These percentages also agree with values obtained by TGA. The total contents of organic elements (C, H, and N) were ca. 4.35 wt% in Zn400, ca. 1.60 wt% in Zn500 and 0.44 wt% in Zn600, indicating that the calcined samples still contain some residual organic matter depending on a calcination temperature. Thus, the transformation of the $ZnS(en)_{0.5}$ complex during calcinations was investigated through TGA and DTA analyses and FT-IR measurements.

In the TGA curve in Fig. 3, the initial drastic weight loss near 300 °C and the second slow weight loss from 350 to 540 °C can be attributed to the thermal decomposition of ethylenediamine in the $ZnS(en)_{0.5}$ complex. The net weight loss up to 540 °C for $ZnS(en)_{0.5}$ is ca. 22.0 wt%, which is also consistent with the theoretical content (23.62 wt%) of ethylenediamine in the complex [11]. The third weight loss from 540 to 625 °C is due to the oxidation of ZnS nanoplates. The DTA curve could be interpreted considering the morphological evolution described below. Thus the exothermal peak around 370 °C is attributed to the transformation of the $ZnS(en)_{0.5}$ to porous wurtzite ZnS

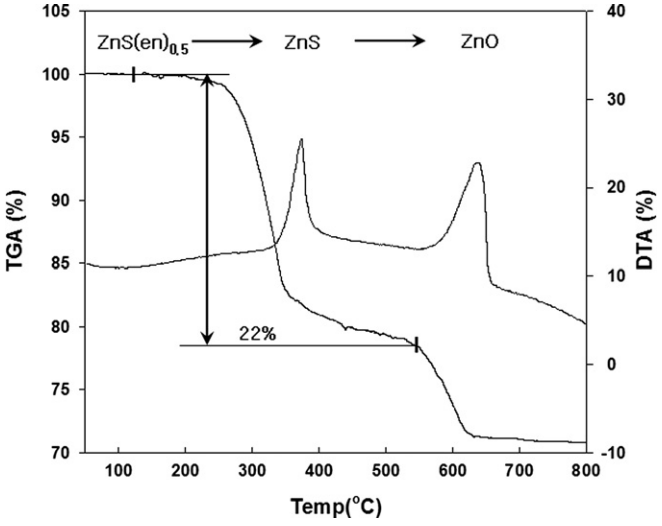

Fig. 3. TGA and DTA curves of the $ZnS(en)_{0.5}$ complex. The TGA was operated in the range of 50 to 800 °C at a heating rate of 10 °C/min under air flow of 45 mL/min.

nanoplates by the thermal decomposition of ethylenediamine in the $ZnS(en)_{0.5}$. The exothermal peak around 630 °C is attributed to the transformation of ZnS to hexagonal ZnO crystallites while maintaining the platelet morphology.

Fig. 4 shows the FT-IR spectra of (a) the $ZnS(en)_{0.5}$ precursor, (b) Zn400, (c) Zn500, and (d) ZnS600. The $ZnS(en)_{0.5}$ spectrum had the NH_2 scissors and twist bands at 1574 and 1020 cm^{-1}, respectively. The CH_2 twist, wag and scissors bands caused absorption at 1075, 1360, 1470 and 2900–3100 cm^{-1}, respectively. The C=C stretching band appeared at 1310–1560 cm^{-1}. After the complex was calcined at 400–600 °C, the absorption peaks disappeared, indicating that ethylenediamine in the $ZnS(en)_{0.5}$ was thermally decomposed and removed from the sample. However, the samples calcined at 400–500 °C still have NH_2 bands around 1020, 1560–1650 cm^{-1}, a C–N band around 1020–1150 cm^{-1}, a broad weak band of C=C stretching at 1310–1560 cm^{-1}, and a new C–O bending band around 1140–1285 cm^{-1}. Thus, although ethylenediamine in the $ZnS(en)_{0.5}$ was thermally decomposed so that its CH_2 bond disappeared, the nitrogen of NH_2 still remained bonded to Zn in ZnS monolayers. A strong bending

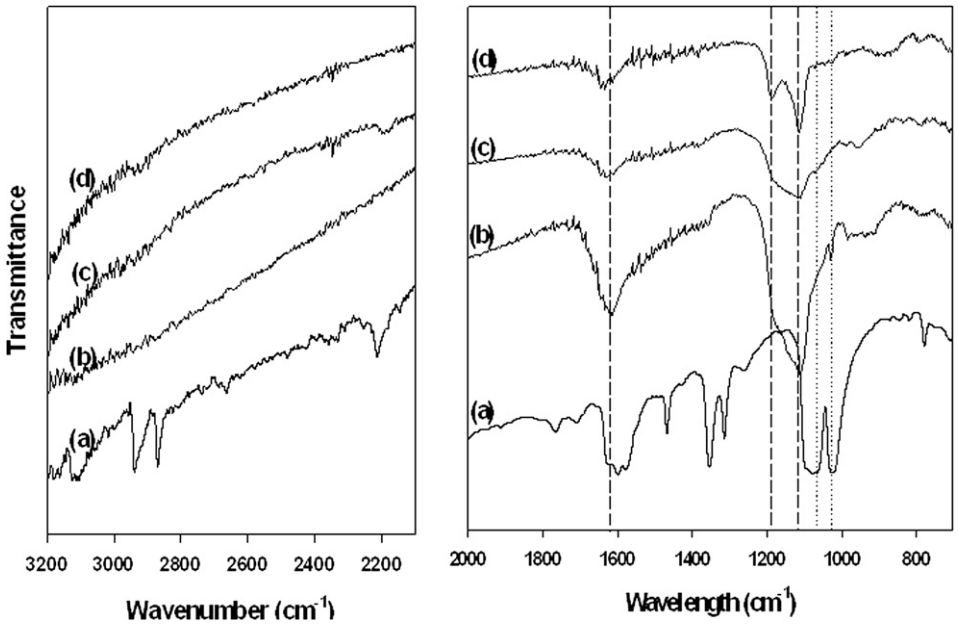

Fig. 4. FT-IR spectra of the $ZnS(en)_{0.5}$ complex and its derivatives calcined at different temperatures; (a) $ZnS(en)_{0.5}$, (b) Zn400, (c) Zn500, and (d) Zn600.

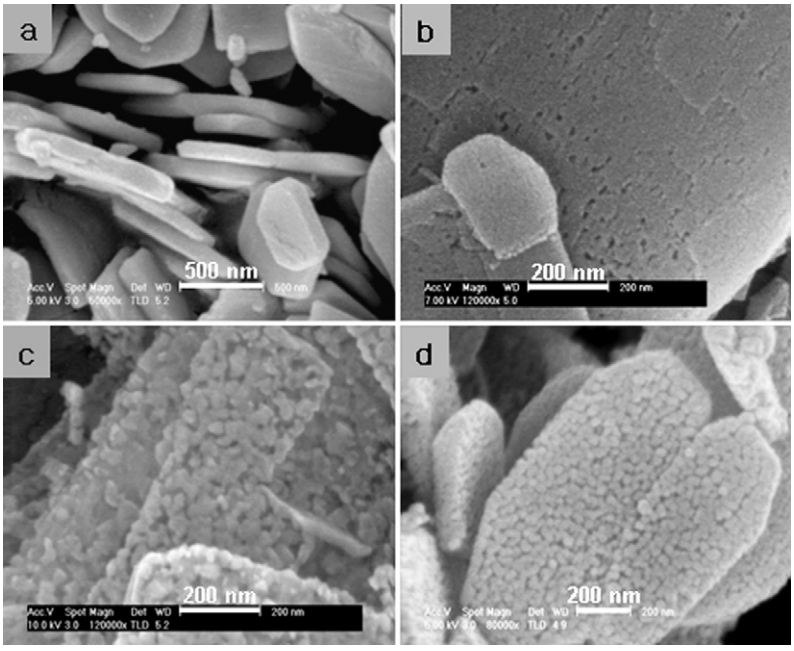

Fig. 5. SEM images of the materials calcined at different temperatures: (a) Zn400, (b) Zn500, (c) Zn550, and (d) Zn600.

vibration at 1630 cm^{-1} and a broad stretching vibration around 3400 cm^{-1} in the spectra of Zn500 and Zn600 suggest the presence of water absorbed from atmosphere.

Fig. 5 shows SEM images of the $ZnS(en)_{0.5}$-derivatives (Zn400, Zn500, Zn550, and Zn600) calcined at indicated temperatures. The apparent features of all samples are similar in that they have stacks of nanoplates with a lateral size of 1–2 μm. The plane surfaces, however, appear to be different: smooth for Zn400, a little porous for Zn500, and highly porous for Zn550 and Zn600. It should be noted that the particle size calculation by the Lorentzian fit for the SR-XRD pattern in Fig. 1b indicates that Zn400 is composed of particles elongated along the *c*-axis 20–30 nm in size. This result is in accord with the TEM image shown in Fig. 6. More discussion on the structure of these porous platelets follows in the next subsection. The observed grain sizes of Zn550 and Zn600 are compatible with the values calculated from powder XRD. Together, TGA and DTA results show that the drastic weight loss near 370 °C does not affect the surface morphology much, but the slow weight loss from 370 to 540 °C is critical in the generation of pores in the samples. The TEM image of Zn400 in Fig. 6a reveals that fine pores are formed in a plate-like particle by the initial removal of ethylenediamine. The selected area electron diffraction (SAED) pattern inserted in Fig. 6a shows bright diffraction

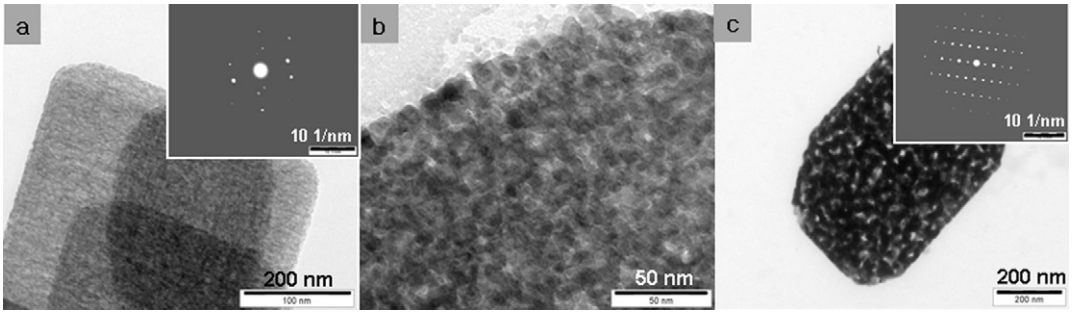

Fig. 6. TEM images of (a) Zn400, (b) Zn500, and (c) Zn600. SAED patterns are shown as insets for samples (a) and (c).

Table 2
Pore structure parameters of the precursor and samples calcined at different temperatures

Sample	Total surface area (m^2/g)	Total pore volume (cm^3/g)	Micropore surface area (m^2/g)	Mesopore surface area (m^2/g)
$ZnS(en)_{0.5}$	10.0	0.03	1.55	8.45
Zn400	27.0	0.06	4.88	22.12
Zn500	34.6	0.10	4.61	30.0
Zn600	32.60	0.21	5.84	26.76

spots, indicating that Zn400 is a single crystal of wurtzite ZnS structure. This result is in accordance with the XRD result of Fig. 1b. Zn500 consists of dominant wurtzite ZnS and a small amount of hexagonal ZnO. It possesses a platelet morphology composed of nanocrystallites and non-uniform pores as shown in Fig. 6b. Further increase of calcination temperature to 600 °C produced fully oxidized ZnO nanocrystallites as shown in the SAED pattern (inset of Fig. 6c) and XRD pattern (Fig. 1e). Yet, the single-crystal hexagonal ZnO maintained the porous platelet morphology of ZnS.

N_2 adsorption/desorption isotherms are shown in Fig. 7A for the $ZnS(en)_{0.5}$ precursor and the samples calcined at different temperatures. The $ZnS(en)_{0.5}$ precursor did not produce a hysteresis loop, but as the calcination temperature increases, the sample develops adsorption/desorption isotherms characteristic of mesoporous materials. The Zn500 and Zn600 samples exhibit similar isotherm patterns corresponding to Type IV hysteresis, which is associated with slit-shaped pores or the space between parallel plates [32]. The hysteresis in the isotherm is probably caused by the pores formed between the laterally-interconnected nanocrystallites. Pore size distribution curves of the samples are shown in Fig. 7B. The $ZnS(en)_{0.5}$ precursor had virtually no pores, whereas Zn400 had small pores of ca. 3.5 nm in average diameter. However, Zn500 had a broad pore size distribution from 3 to 15 nm and Zn600 had a narrower distribution of larger pores of 10–30 nm. This result indicates that thermal-treatment at a high temperature of 600 °C is essential to make porous plates having large and uniform pores. The pore structure parameters of the samples are summarized in Table 2. After calcination of the $ZnS(en)_{0.5}$ precursor, the total surface area and pore volume increased by more than a factor of three, which is attributed to the pores formed by the removal of ethylenediamine and space between interconnected nanocrystalline particles.

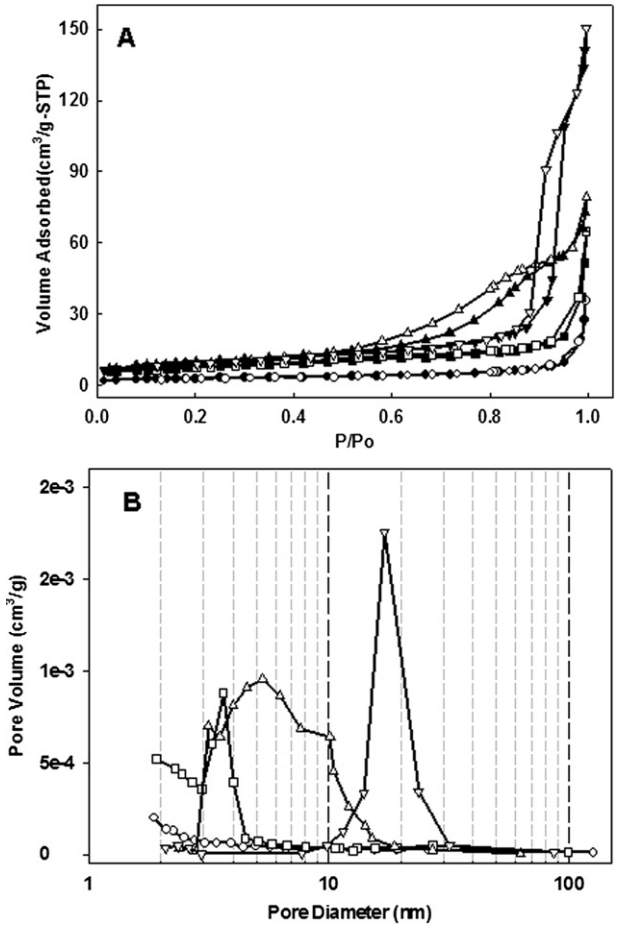

Fig. 7. (A) N_2 adsorption–desorption isotherms and (B) pore size distributions calculated by the BJH method from the desorption branch of the N_2 isotherm for $Zn(en)_{0.5}$ (○, ●), Zn400 (□, ■), Zn500 (△, ▲), and Zn600 (▼, ▽). Filled and empty symbols denote adsorption and desorption branches of N_2 isotherms, respectively.

The evolution of structure, morphology and texture involved in the solid transformation of $ZnS(en)_{0.5} \rightarrow ZnS \rightarrow ZnO$ reveals that the transformation is *topotatic*. ZnS and ZnO share the same hexagonal crystal structure throughout the bulk of the solid derived from orthorhombic $ZnS(en)_{0.5}$, satisfying the definition of topotaxy [33,34]. Thus, during the processes of $ZnS(en)_{0.5}$ decomposition to ZnS and transformation of ZnS to ZnO, Zn atoms move minimally. This highly limited movement of Zn atoms during the whole two-step solid transformation is responsible for the pseudomorphism, i.e. retention of

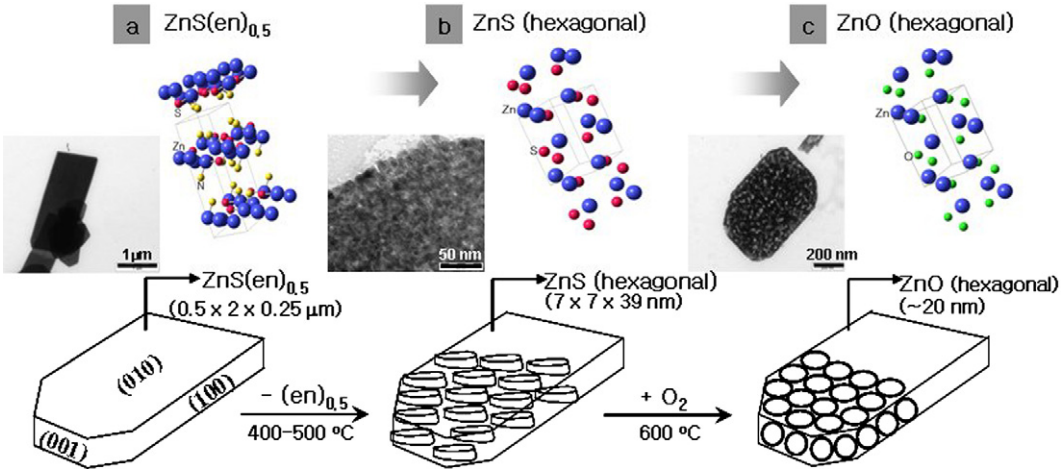

Fig. 8. Scheme of the topotactic solid transformation of a platelet of $ZnS(en)_{0.5}$ to mesoporous ZnS nanoplates, and then to mesoporous ZnO nanoplates.

the platelet morphology, despite the drastic decrease in crystal sizes.

The processes are illustrated in Fig. 8. In the first step of $ZnS(en)_{0.5}$ decomposition, ZnS retains the external shape and dimensions of the particles of $ZnS(en)_{0.5}$, although the composition, crystal size, and density have been greatly changed. A platelet of single crystal $ZnS(en)_{0.5}$ with dimensions of approximately $0.5 \times 2 \times 0.25$ μm in the of [100], [001], and [010] directions, respectively, exposes the extended (010) plane of the orthorhombic unit cell. This $ZnS(en)_{0.5}$ platelet is converted to a platelet of the similar size and shape, but now consisting now of many ZnS crystals approximately $7 \times 7 \times 39$ nm. The loss of ethylenediamine molecules must be balanced by the formation of internal pores in order to retain the original shape and size. Thus, the material, originally nonporous, develops pores. A large increase in specific surface area also follows, as shown in Table 2. The sulfide-to-oxide transformation appears much simpler, involving only the exchange of non-metal atoms. Thus, S atoms diffuse out and O atoms move in to take their places. However, the primary ZnO particles become more isotropic and grow in size above 20 nm. This suggests the substantial movement of Zn atoms at high temperatures. There is also a small decrease in the specific volume when the larger S atoms are replaced by the smaller O atoms. As a result, there is a further increase in the pore volume, pore size, and surface area during the sulfide-to-oxide transformation.

An interesting observation from Fig. 6 is that the SAED patterns for a single platelet are spots instead of rings. Because the platelet is the aggregate of ZnS or ZnO crystals of much smaller dimensions, ring patterns are expected if the crystals are randomly oriented to each other. The observed spot patterns indicate that the individual crystallites forming a platelet are oriented in such a way that the relative positions of Zn are the same as in the original $ZnS(en)_{0.5}$ platelet, as if they still belong to a single large crystal. Although the single crystal of $ZnS(en)_{0.5}$ is broken into many ZnS or ZnO crystals during the $ZnS(en)_{0.5} \rightarrow ZnS \rightarrow ZnO$ transformation, these crystals form an aggregate of the same shape as the $ZnS(en)_{0.5}$ platelet and the relative positions of Zn remain unaltered as far as the crystals remaining in the same aggregate. In this sense, ZnS and ZnO platelets could be called "highly porous single crystals". This is convincing evidence that shows topotatic transformation has indeed taken place [35].

3.2. Structures of grains in porous plates

XAFS was applied to investigate the structure of grains generated due to calcination at high temperatures. It provides direct information on the electronic and geometric structures around a central absorbing atom in a local order and thus, can be complementary to powder XRD. Fig. 9A displays Zn K-edge XANES of $ZnS(en)_{0.5}$ (a), Zn400 (b), Zn500 (c), and bulk ZnS (d). We found that the XANES features of Zn400 and Zn500 are closer to those of $ZnS(en)_{0.5}$, rather than those of bulk ZnS. This result is inconsistent with the SR-XRD results in Fig. 1, b and c. As the organic component of $ZnS(en)_{0.5}$ decomposes near 370 °C, the crystalline form of $ZnS(en)_{0.5}$ becomes amorphous, and crystallites of wurtzite ZnS are slowly formed. Yet, some of layers may still be combined with nitrogen atoms from ethylenediamine, making the environment of some Zn atoms in Zn400 and Zn500 similar to that of $ZnS(en)_{0.5}$. This is consistent with FT-IR results in Fig. 4. On the other hand, Fig. 9B shows that the Zn K-edge XANES spectra of grains produced by calcinations at 550 and 600 °C are almost the same as that of bulk ZnO.

EXAFS analyses for the $ZnS(en)_{0.5}$, Zn400, and Zn500 are shown in the inset of Fig. 9A. The RSF (amplitude functions of Fourier-transformed data) for Zn400 and Zn500 show features now similar to that of ZnS rather than $ZnS(en)_{0.5}$, especially in distances of $R > 3$ Å. We could identify the backscattering element contributing to a given peak by examining the imaginary functions in the Fourier-transformed spectra [26,36,37]. In Fig. 10, the first shells at 0.7–2.2 Å for all samples show the same imaginary function features, i.e., the same number of the peaks and very similar positions of the peaks. With the FEFF calculation for bulk wurtzite ZnS, the first shell can be assigned to the contribution from the four nearest sulfur atoms. In the case of the $ZnS(en)_{0.5}$, the first shell comprises three sulfur atoms and one nitrogen atom from ethylenediamine [29]. It is well known that a lighter backscatterer is hard to identify if

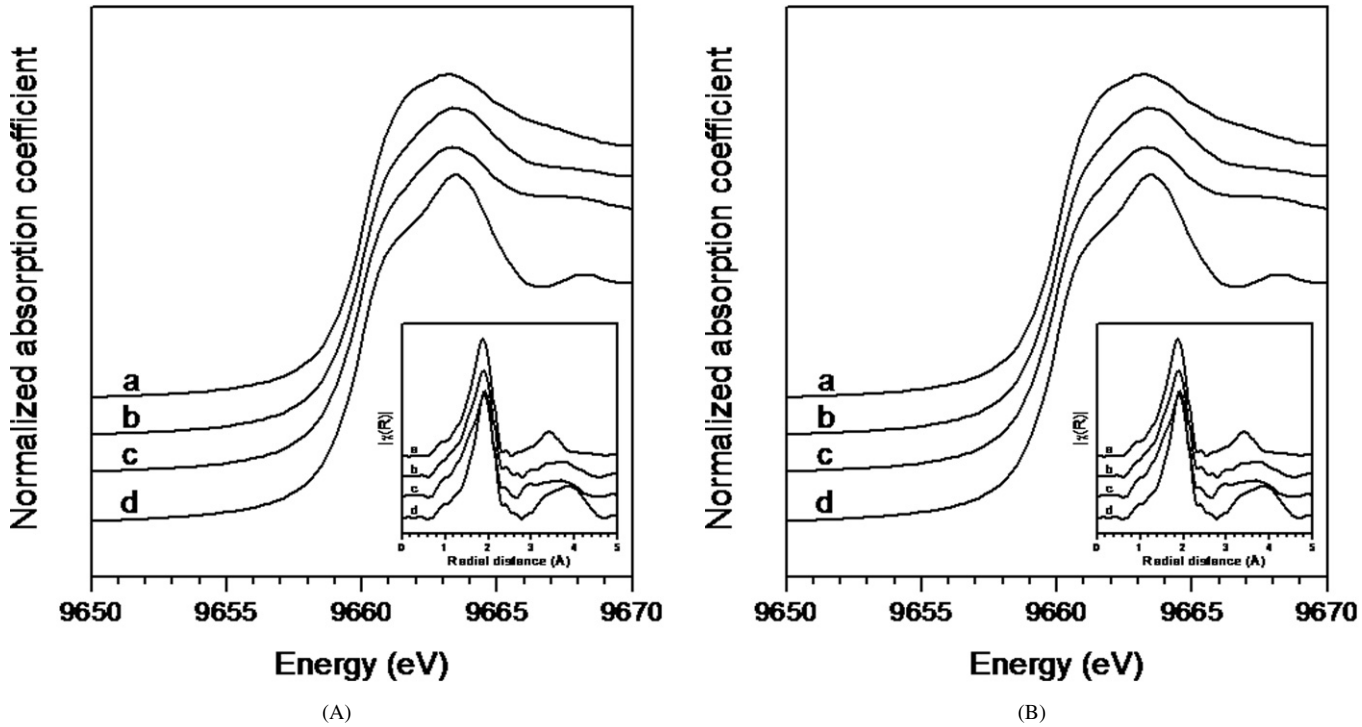

Fig. 9. Zn K-edge XANES spectra of the $ZnS(en)_{0.5}$, its calcined derivatives, and reference materials (A): (a) $ZnS(en)_{0.5}$, (b) Zn400, (c) Zn500, and (d) bulk ZnS; and (B): (a) Zn550, (b) Zn600, and (c) bulk ZnO. Inset plots are their respective Fourier-transformed RSF spectra.

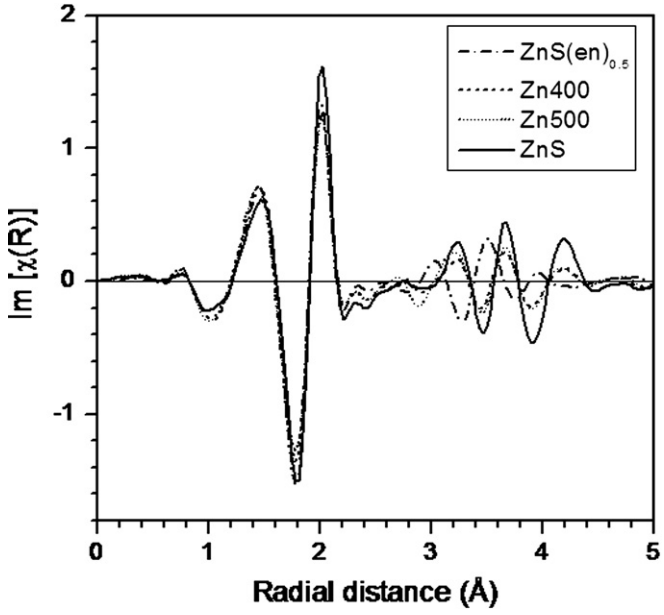

Fig. 10. Imaginary functions of Fourier-transformed $k^3\chi(k)$ for the $ZnS(en)_{0.5}$ precursor, Zn400, Zn500, and bulk ZnS.

its bond distance is not much different from others. For the features of the higher shells at 2.2–4.3 Å, the samples Zn400 and Zn500 basically show the same imaginary functions as that of ZnS (except peak intensity), not that of the $ZnS(en)_{0.5}$. However, for Zn550 and Zn600, their RSF (the inset of Fig. 9B) and imaginary functions in the Fourier-transformed spectra (not shown) are exactly the same as that of bulk ZnO up to 6 Å. Therefore, based also on XANES results, the grains in Zn400 and Zn500 can be described as ZnS nanoparticles embedded in amorphous intermediates derived from the $ZnS(en)_{0.5}$ complex. In contrast, Zn550 and Zn600, as revealed in powder diffraction, are fully oxidized ZnO nanocrystallites having the same structures as bulk ZnO.

3.3. Photocatalytic performance

Before investigating the photocatalytic performance of the materials, their optical properties were examined by UV–vis diffuse reflection (UV-DR). Fig. 11 shows UV-DR spectra of the $ZnS(en)_{0.5}$ complex, Zn400, Zn500, Zn550, and Zn600. The $ZnS(en)_{0.5}$ has a sharp edge at 260 nm, which is blue-shifted by about 1.2 eV with respect to bulk wurtzite ZnS. Zn400 and Zn500 have spectra similar to that of bulk ZnS but with broad absorption shoulders over the region of 400–800 nm. The shoulder can be due to crystal defects or amorphous phases. It has been reported that the doping of nitrogen into substitutional sites of TiO_2 at ambient or high temperature conditions can extend absorption onset into the visible region to 520 nm and cause photocatalytic activity under visible light [38–40]. However, the shoulder in this study is more likely due to the amorphous $ZnS(en)_{0.5}$ remnants and carbon doping into the site of ZnS during calcination process. Since Zn400 and Zn500 samples consist of wurtzite ZnS nanoparticles and amorphous intermediates derived from $ZnS(en)_{0.5}$ as discussed above, the amorphous phase would decrease as the calcination temperature increases from 400 to 500 °C. This is indeed what is observed, as Zn500 has a reduced shoulder. This observation supports our suggestion that amorphous $ZnS(en)_{0.5}$ remnants are present in Zn400 and Zn500. The insets of Fig. 11A and 11B show the ap-

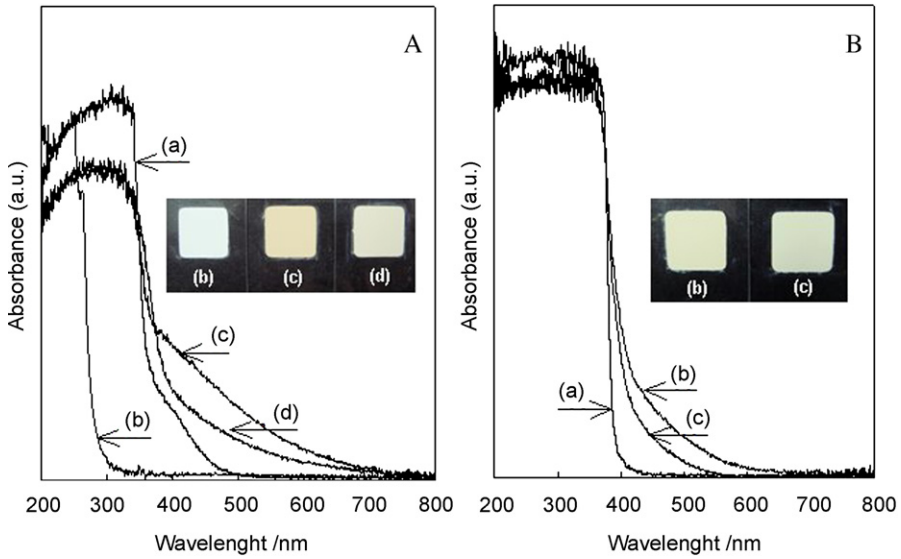

Fig. 11. UV–vis diffuse reflectance spectra of (A): (a) bulk ZnS(wurtzite), (b) $ZnS(en)_{0.5}$ precursor, (c) Zn400, (d) Zn500, and (B): (a) ZnO, (b) Zn550, (c) Zn600. Insets show the color of the samples.

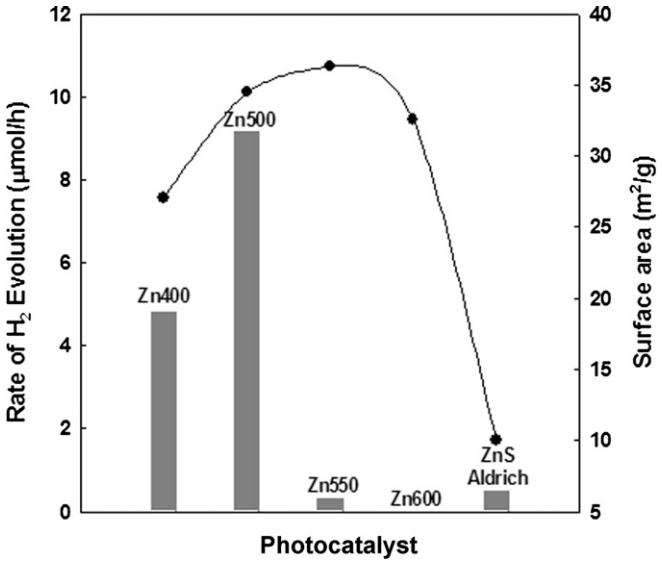

Fig. 12. Hydrogen production rates of the $ZnS(en)_{0.5}$-derivatives calcined at different temperatures. Catalysts: 0.1 g loaded 1 wt% Pt. Electrolyte: 0.1 M $Na_2S + 0.02$ M Na_2SO_3. Light source: Hg-arc lamp (500 W) equipped with IR liquid filter and UV cut-off filter ($\lambda \geqslant 420$ nm). BET surface area is also plotted as the solid line.

parent colors of the precursor and the calcined samples, which are related to the absorption property of the samples. Commercial bulk ZnS and ZnO (not shown) are white powders.

Fig. 12 displays the evolution rates of H_2 from an aqueous solution containing 0.1 M Na_2S and 0.02 M Na_2SO_3 as sacrificial reagents under visible light irradiation ($\lambda \geqslant 420$ nm) for various samples and their specific BET surface areas. Zn500 had the highest rate of hydrogen evolution. ZnO nanocrystallites in Zn550 and Zn600 did not produce hydrogen under visible light. In general, ZnS is a semiconductor with a wide direct bandgap (3.80 eV), which does not produce hydrogen under visible light. As mentioned above, $ZnS(en)_{0.5}$-derivatives calcined at 400–500 °C absorb visible light as indicated by the absorption shoulders in Fig. 10, so they could have photocatalytic activity under visible light. The Zn500 sample, with the largest visible light absorption, exhibited the highest hydrogen production rate. There is no obvious correlation between the surface area and photocatalytic activity.

Fig. 13A shows time curves of the photocatalytic hydrogen production for 12 h with intermittent N_2 gas purging every 3 h (dotted line). There was no noticeable decrease of activity during the first two runs for 6 h. But, from the third run, the photocatalytic activity for hydrogen evolution decreased noticeably. The catalyst structure did not change during the photoreaction for 12 h as shown by XRD patterns in Fig. 13B. In addition, we measured FT-IR spectra of Zn550 sample catalysts before and after photocatalytic reaction of dye decomposition. There was no additional IR band in the used sample due to charge-containing intermediates such as carboxylate, acetate, and formate, which are reported to deactivate TiO_2 photocatalysts [41]. Thus, the decrease in the rate of hydrogen evolution in Fig. 13A is not due to the instability of photocatalyst, but due to the consumption of the sacrificial reagents in the electrolyte solution.

Fig. 14A shows the wavelength-dependence on the photocatalytic hydrogen production over Zn500. The photocatalytic activity for hydrogen evolution decreases with increasing wavelength because the number of available photons decreased [42]. This result indicates that the light absorbed by Zn500 is responsible for its activity for the photoreaction. The XPS data suggest the reason why Zn500 could absorb the visible light. The C 1s XPS spectrum of Zn500 showed a large peak at 284.6 eV and a broad peak in the energy range of 280–284 eV, as shown in Fig. 14B. The sharp peak at 284.6 eV can be attributed to free carbon and the broad peak around 280–284 eV could be assigned to carbon interacting with Zn through Zn–C bond formation [43]. Based on the photocatalytic activity and XPS data, we proposed the schematic band structure of Zn500 sample shown in Fig. 14C. Thus, participation of C 2p orbital

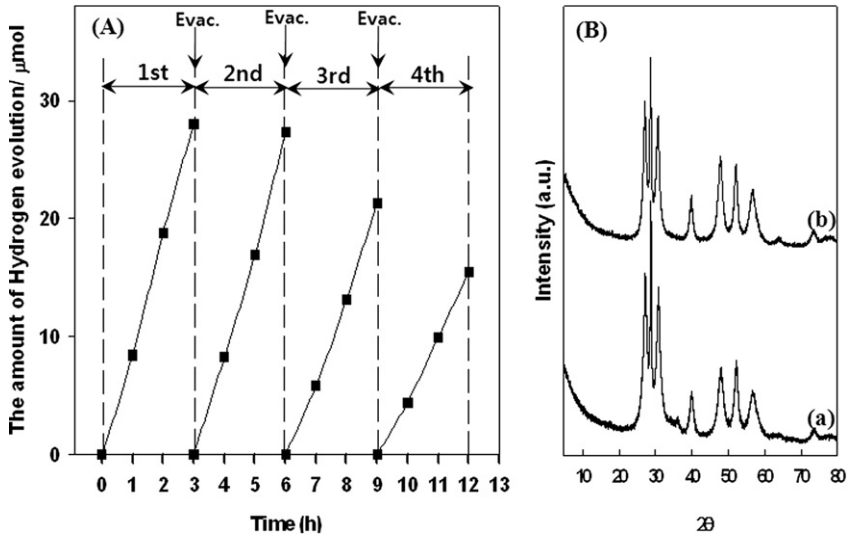

Fig. 13. (A) Time course of hydrogen production under visible light irradiation ($\lambda \geqslant 420$ nm) on Zn500. The reaction was continued for 12 h with intermittent evacuation every 3 h. (B) XRD patterns of 1 wt% Pt loaded Zn500 before and after photocatalytic reaction.

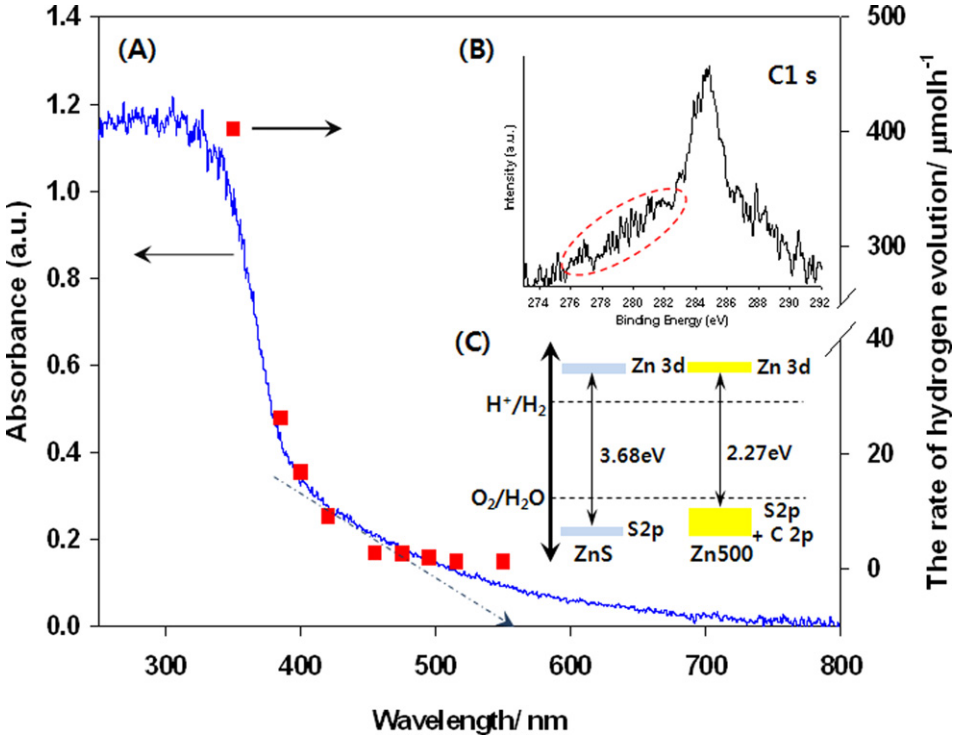

Fig. 14. (A) The rates hydrogen evolution (square points) vs the wavelengths of cut-off filters over Zn500 sample. Catalysts: 0.1 g loaded 1 wt% Pt. Electrolyte: 0.1 M Na_2S + 0.02 M Na_2SO_3. Light source: Hg-arc lamp (500 W) equipped with IR liquid filter and UV cut-off filter ($\lambda \geqslant 420$ nm). Optical absorption spectrum of the sample is also shown for comparison. (B) The XPS core-level spectrum of C 1s in Zn500 sample. (C) The proposed band structure of Zn500 sample.

in the formation of the top of the valence band may be responsible for the reduced band gap and visible light absorption of Zn500.

The catalytic performance under UV-light irradiation ($\lambda \geqslant 324$ nm) was also examined for photocatalytic degradation of azo dye acid red 14 (AR14) to gauge the oxidation capability of ZnO-based photocatalysts (Zn550, Zn600). The plot inserted in Fig. 15 illustrates typical time-dependent UV–vis spectra of AR14 solution during photocatalytic degradation. The spectra of AR14 in the visible region exhibit a main band with a maximum at $\lambda_{max} \sim 515$ nm. The absorption peaks of AR14 gradually decreased and finally disappeared during the photocatalytic reaction. The degradation rates of AR14 over Zn550 and Zn600 are so high that less than 10% of AR14 remained after UV-irradiation for 100 min. The activity is comparable with that of the commercial bulk ZnO. Therefore, the $ZnS(en)_{0.5}$ derivatives calcined at 550–600 °C are plausible candidates for the degradation of toxic organic materials under UV light.

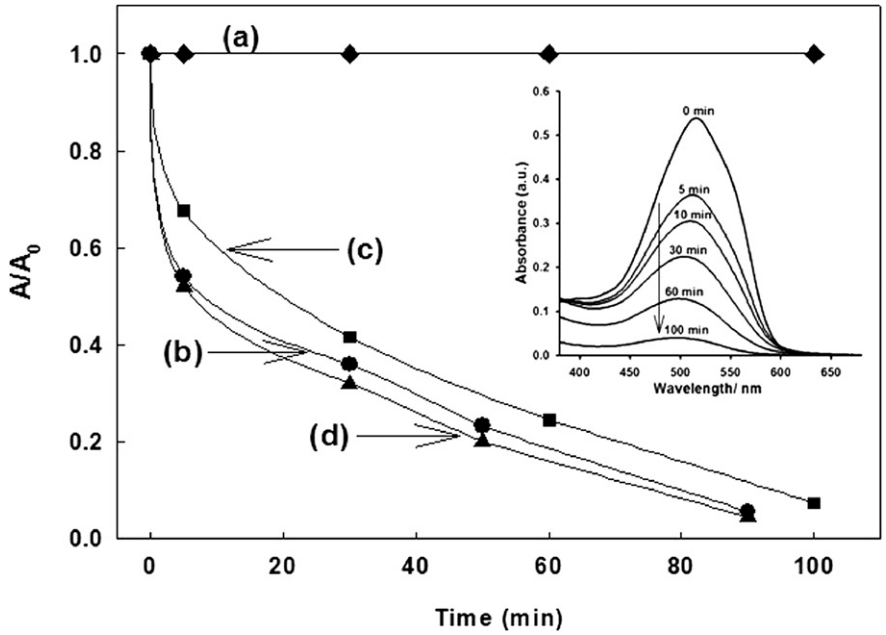

Fig. 15. Photocatalytic decomposition of azo dye acid red 14 (AR 14) under UV light: (a) no catalyst, (b) Zn550, (c) Zn600, and (d) bulk ZnO. Catalysts: 50 mg. AR 14 solution: A 100 mL of 50 μM AR 14. Light source: Hg-arc lamp (500 W) equipped with IR liquid filter and UV cut-off filter ($\lambda \geqslant 324$ nm). A is the absorbance of AR 14 ($\lambda_{max} = 515$ nm) and A_0 is the initial absorbance. The inset figure indicates a typical spectral change with irradiation time.

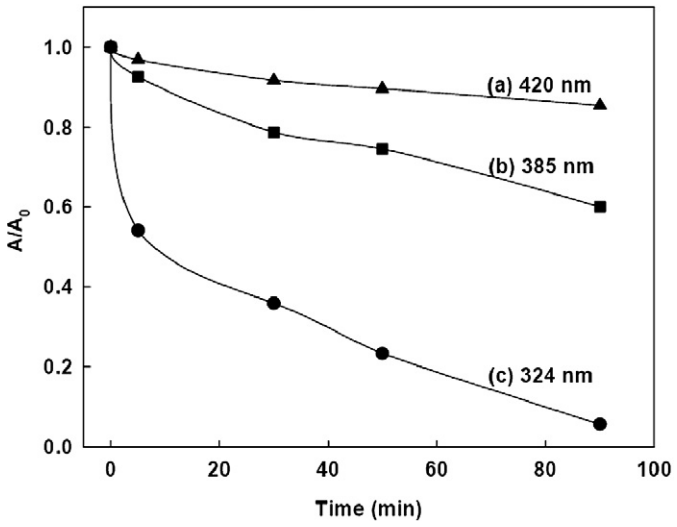

Fig. 16. Photocatalytic decomposition of azo dye acid red 14 (AR 14) vs the wavelengths of cut-off filters over Zn500 sample: (a) 324, (b) 385, and (c) 420 nm. Catalysts: 50 mg. AR 14 solution: A 100 mL of 50 μM AR 14. Light source: Hg-arc lamp (500 W) equipped with IR liquid filter and UV cut-off filter ($\lambda \geqslant 324$ nm). A is the absorbance of AR 14 ($\lambda_{max} = 515$ nm) and A_0 is the initial absorbance.

We measured the photocatalytic activity for dye decomposition under visible light irradiation with cut off filters ($\lambda \geqslant 324$, 385, and 420 nm). Although the degradation rates of AR 14 over Zn550 under visible irradiation ($\lambda \geqslant 385$ and 420 nm) are lower than that of Zn550 under UV irradiation ($\lambda \geqslant 324$), mesoporous Zn550 nanoplate shows the photocatalytic ability for dye decomposition under both UV and visible light irradiation as shown in Fig. 16.

4. Conclusions

A $ZnS(en)_{0.5}$ complex in a platelet morphology with a lateral dimension of 1–2 μm and a smooth surface was successfully synthesized via a solvothermal route using ethylenediamine as a single solvent at 160 °C. The thermal decomposition of the complex produced porous ZnS and ZnO by a topotatic solid transformation. Thus, the plate-like morphology was preserved throughout the process, but the ZnS and ZnO platelets were porous and surface area increased drastically. At calcination temperatures of 400–500 °C, the grains in the porous plates appear to be composed of wurtzite ZnS nanocrystallites embedded in the amorphous $ZnS(en)_{0.5}$ remnants considering SEM, SR-XRD, FT-IR, and elemental analysis data. Further oxidation at 550–600 °C transformed them to ZnO nanocrystallites. The ZnS-based samples calcined below 500 °C demonstrated good photocatalytic acitivities for hydrogen production from aqueous solutions of sacrificial reagents under visible light irradiation ($\lambda \geqslant 420$ nm), whereas ZnO-based samples calcined above 550 °C exhibited high photocatalytic activity in the decomposition of the azo dye (AR14) under UV-light irradiation ($\lambda \geqslant 324$ nm).

Acknowledgments

This work was supported by the Hydrogen Energy R&D Center, a 21st Century Frontier R&D Program funded by the Ministry of Science and Technology of Korea, and the Brain Korea 21 Program of the Ministry of Education of Korea. Powder X-ray diffraction and XAFS experiments at PAL were supported in part by MOST and POSTECH.

References

[1] M. Ihara, T. Igarashi, T. Kusunoki, K. Ohno, J. Electrochem. Soc. H 72 (2002) 149.
[2] S. Yanagida, K. Mizumoto, C.J. Pac, J. Am. Chem. Soc. 108 (1986) 647.
[3] S. Yanagida, T. Azuma, Y. Midori, C.J. Pac, H. Sakurai, J. Chem. Soc. Perkin Trans. 2 (1985) 1487.
[4] X. Wang, P. Gao, J. Li, C.J. Summers, Z.L. Wang, Adv. Mater. 14 (2002) 1732.
[5] E. Comini, G. Faglia, G. Sberveglieri, Z. Pan, Z.L. Wang, Appl. Phys. Lett. 81 (2002) 1869.
[6] C. Ye, Y. Bando, G. Shen, D. Golberg, J. Phys. Chem. B 110 (2006) 15146.
[7] M.L. Curri, R. Comparelli, P.D. Cozzoli, G. Mascolo, A. Agostiano, Mater. Sci. Eng. C 23 (2003) 285.
[8] A.J. Hoffman, E.R. Carraway, M.R. Hoffmann, Environ. Sci. Technol. 28 (1994) 776.
[9] E.R. Carraway, A.J. Hoffman, M.R. Hoffmann, Environ. Sci. Technol. 28 (1994) 786.
[10] S.H. Yu, M. Yoshimura, Adv. Mater. 14 (2002) 296.
[11] Z.X. Deng, C. Wang, X.M. Sun, Y.D. Li, Inorg. Chem. 41 (2002) 869.
[12] S.H. Yu, J. Yang, Y.T. Qian, M. Yoshimura, Chem. Phys. Lett. 361 (2002) 362.
[13] G.H. Yue, P.X. Yan, D. Yan, J.Z. Liu, D.M. Qu, Q. Yang, X.Y. Fan, J. Cryst. Growth 293 (2006) 428.
[14] X. Quyang, T.Y. Tsai, D.H. Chen, Q.J. Huang, W.H. Cheng, A. Clearfield, Chem. Commun. (2003) 886.
[15] G.T. Zhou, X. Wang, J.C. Yu, Cryst. Growth Des. 5 (2005) 1761.
[16] J. Dai, Z. Jiang, W. Li, G. Bian, Q. Zhu, Mater. Lett. 55 (2002) 383.
[17] H. Yin, Y. Wada, T. Kitamura, S. Yanagida, Environ. Sci. Technol. 35 (2001) 227.
[18] Y. Wada, H. Yin, T. Kitamura, S. Yanagida, Chem. Commun. (1998) 2683.
[19] C.L. Torres-Martinez, R. Kho, O. Mian, R.K. Mehra, J. Colloid Interface Sci. 240 (2001) 525.
[20] X. Wang, S.O. Pehkonen, A.K. Ray, Ind. Eng. Chem. Res. 43 (2004) 1665.
[21] J.S. Hu, L.L. Ren, Y.G. Guo, H.P. Liang, A.M. Cao, L.J. Wan, C.L. Bai, Angew. Chem. Int. Ed. 44 (2005) 1269.
[22] A.L. Ankudinov, C. Bouldin, J.J. Rehr, J. Sims, H. Hung, Phys. Rev. B 65 (2002) 104107.
[23] M. Newville, J. Synch. Rad. 8 (2001) 322.
[24] S.H. Choi, J.S. Lee, J. Catal. 167 (1997) 364.
[25] E.D. Park, S.H. Choi, J.S. Lee, J. Phys. Chem. B 104 (2000) 5586.
[26] D.E. Sayer, B.A. Bunker, in: D.C. Koningsberger, R. Prins (Eds.), X-Ray Absorption: Principles, Applications, Techniques of EXAFS, SEXAFS and XANES, Wiley, New York, 1988, p. 211.
[27] M. Kruk, M. Jaroniec, A. Sayari, Langmuir 13 (1997) 6267.
[28] E.P. Barett, L.G. Joyner, P.P. Halender, J. Am. Chem. Soc. 73 (1951) 373.
[29] X. Ouyang, T.Y. Tsai, D.H. Chen, Q.J. Huang, W.H. Cheng, A. Clearfield, Chem. Commun. (2003) 886.
[30] A. Guinier, X-Ray Diffraction, Dover Publications, New York, 1963, p. 124.
[31] J.B. Hastings, W. Thomlinson, D.E. Cox, J. Appl. Phys. 17 (1984) 85.
[32] K.S.W. Sing, D.H. Evertt, R.A.W. Haul, L. Moscou, R.A. Pierotti, J. Rouquerol, T. Siemieniewska, Pure Appl. Chem. 57 (1985) 603.
[33] J.S. Lee, L. Volpe, F.H. Ribeiro, M.J. Boudart, J. Catal. 112 (1988) 44.
[34] L. Volpe, M. Boudart, Catal. Rev. Sci. Eng. 27 (1985) 515.
[35] J.S. Lee, Korean J. Chem. Eng. 6 (1989) 196.
[36] S.H. Choi, W.R. Benjamin, J.A. Ryder, A.T. Bell, J. Phys. Chem. B 107 (2003) 11843.
[37] M. Vaarkamp, Catal. Today 39 (1998) 271.
[38] R. Asahi, T. Morikawa, T. Ohwaki, K. Aoki, Y. Taga, Science 293 (2001) 269.
[39] J.L. Gole, J.D. Stout, C. Burda, Y. Lou, X. Chen, J. Phys. Chem. B 108 (2004) 1230.
[40] M. Mrowetz, W. Balcerski, A.J. Colussi, M.R. Hoffmann, J. Phys. Chem. B 108 (2004) 17270.
[41] Z. Yu, S.S.C. Chuang, J. Catal. 246 (2007) 118.
[42] S.M. Ji, P.H. Borse, H.G. Kim, D.W. Hwang, J.S. Jang, S.W. Baea, J.S. Lee, Phys. Chem. Chem. Phys. 7 (2005) 1315.
[43] H. Pan, J.B. Yi, L. Shen, R.Q. Wu, J.H. Yang, J.Y. Lin, Y.P. Feng, J. Ding, L.H. Van, J.H. Yin, J. Catal. 99 (2007) 127201.